SIMULTANEOUS DCE-DSC-MRI USING LOW-RANK-REGULARIZED MODEL-BASED RECONSTRUCTION OF DCE AND DSC COMPONENTS

Marie Mangová, Pavel Rajmic

Brno University of Technology
FEEC, Dept. of Telecommunications
Technická 12, 616 00 Brno, Czech Republic

Ondřej Macíček, Denisa Hývlová, Radovan Jiřík

Institute of Scientific Instruments
of the Czech Academy of Sciences
Královopolská 147, 612 00 Brno, Czech Republic

ABSTRACT

In quantitative perfusion MRI, reliable estimation of tissue perfusion parameters remains a challenging task. Recently, the simultaneous DCE-DSC-MRI technique has attracted attention since it leads to more reliable estimates of perfusion-parameter maps than DCE- or DSC-MRI alone. In this paper, we propose a method of simultaneous DCE-DSC-MRI based on spatio-temporal locally low-rank regularization of the DCE and DSC image sequences. By comparison with the baseline DCE-DSC-MRI method, we demonstrate improved accuracy of the perfusion-parameter maps. The evaluations are performed on a realistic synthetic phantom of a rat head with several noise levels.

Index Terms— Magnetic resonance imaging; quantitative perfusion analysis; DCE; DSC; low rank; regularization

1. INTRODUCTION

Magnetic resonance imaging (MRI) is currently more and more used for measurement than only as an imaging device. Next to anatomic images, it can measure physical quantities characterizing tissue function. Perfusion MRI is an important group of such measurement methods used for diagnosis and therapy monitoring, especially in oncology [1], as well as in preclinical (small-animal) MRI in the development of new treatment strategies [2]. It provides assessment of the perfusion status of a tissue on the capillary level.

Dynamic Contrast-Enhanced (DCE) MRI and Dynamic Susceptibility-Contrast (DSC) MRI are the most widely used perfusion MRI techniques in oncology. They are based on intravenous administration of a contrast agent (CA) and acquisition of T1-weighted (DCE) or T2(*)-weighted (DSC) image sequence capturing the temporal and spatial distribution of the CA upon its administration. While DCE-MRI is mostly used for the quantification of vessel-wall permeability, DSC-MRI is more suitable for the assessment of blood flow. DCE and DSC data can be acquired simultaneously, using multi-gradient-echo (MGE) acquisition, which captures a set of images with multiple echo times (TEs) for every time instant [3, 4]. The processing of such DCE and DSC data and the complementary advantages of both techniques can be employed to yield more accurate perfusion-parameter estimates than with DCE- or DSC-MRI alone [5, 6, 7].

The first part of simultaneous DCE-DSC-MRI processing is the extraction of the DCE and DSC components from the MGE dataset. The accuracy and precision of this step are crucial for the reliability of the following steps, which consist of fitting the pharmacokinetic and gradient-correction models simultaneously to these DCE and DSC components.

The extraction of DCE and DSC components from MGE data (weighted by both T1 and T2*) is formulated as a separation of the T1 (DCE component) and T2* (DSC component) effects of the CA on the imaged tissue. This is done independently for every voxel and time instant by estimating the DCE component as a T1-weighted image intensity with eliminated T2* effect and the DSC component as T2*. This corresponds to fitting an exponential function to image-intensity versus TE curves. In previous work combining DCE- and DSC-MRI, this exponential-function fitting has always been done independently for each voxel and time instant [3, 4, 8, 5, 6, 7]. In this work, we propose a new approach by including spatio-temporal regularization to achieve more reliable results. We employ low-rank regularization known, for example, in image reconstruction [9, 10, 11, 12] but not in the context of extraction of DCE and DSC components from MGE data for simultaneous DCE-DSC-MRI. We evaluate our method on the whole DCE-DSC-MRI processing chain applied to realistically simulated data and quantify the improvement on the final perfusion-parameter maps.

2. DCE-DSC-MRI ACQUISITION AND ESTIMATION

For simultaneous DCE-DSC-MRI acquisition, the standard MGE method is assumed, as used in [3, 4, 13]. It is based on multi-TE (i.e., acquiring images for multiple TEs) spoiled-gradient-echo acquisition with Cartesian sampling of the *k*-space. The MGE acquisition is repeated to capture a dynamic multi-TE image sequence (several minutes long with the temporal resolution in units of seconds). The acquired *k*-space data are reconstructed using the inverse FFT. Subsequently, assuming a multi-element receiving coil, the sensi-

tivity maps are estimated [14], employed in the reconstruction of $\mathbf{X}_k$, and the magnitude images are used as the input to the procedure extracting the DCE and DSC components.

In the following, the magnitude data will be denoted $|\mathbf{X}_k|$, where k is the index of TE. Each of the data $|\mathbf{X}_k|$ is actually a three-way tensor of size $N_\mathrm{x} \times N_\mathrm{y} \times N_\mathrm{t}$, with N_x and N_y being the image size (we assume imaging a single slice) and N_t represents the number of time-domain frames in the acquired image sequence. In the extraction of the DCE and DSC components, the DCE component is the T1-weighted image sequence with eliminated T2* effect (i.e., an image sequence that would be acquired for hypothetical TE = 0 s), denoted as $\mathbf{A}$ further on. The DSC component corresponds to $1/T2^*$, substituted by $\mathbf{B}$ for simplicity. Both $\mathbf{A}$ and $\mathbf{B}$ are three-way tensors of size $N_\mathrm{x} \times N_\mathrm{y} \times N_\mathrm{t}$, the same as each $|\mathbf{X}_k|$.

Estimation of $\mathbf{A}$ and $\mathbf{B}$ is formulated as a minimization of the following optimization criterion

$$F(\mathbf{A}, \mathbf{B}) = \frac{1}{2} \sum_k \left\| |\mathbf{X}_k| - \mathbf{A} \odot \mathrm{e}^{-\mathbf{B} \cdot TE_k} \right\|_\mathrm{F}^2 +$$
$$+ \lambda_\mathrm{A} \sum_i \left\| D_\mathrm{A}^i \mathbf{A} \right\|_* + \lambda_\mathrm{B} \sum_j \left\| D_\mathrm{B}^j \mathbf{B} \right\|_*. \quad (1)$$

The first summand of the functional is the data fitting term that relates the observation with the parameters $\mathbf{A}$ and $\mathbf{B}$. The expression models the time series $|\mathbf{X}_k|$ as an exponential. The mathematical operations are taken elementwise; the symbol $\odot$ denotes an elementwise multiplication. Echo times of the MGE acquisition are denoted as TE_k. The norm $\|\cdot\|_\mathrm{F}$ is the Frobenius norm over the three-way tensor, an equivalent of the Euclidean norm for vectors.

With this term alone, one could estimate the parameters $\mathbf{A}$ and $\mathbf{B}$ using classic numerical techniques such as nonlinear least squares [15]. This approach will actually serve as the baseline in the comparison (with standard determination of $|\mathbf{X}_k|$ combining magnitude images of the coil elements via the sum of squares, i.e., no estimation of sensitivities). It is a voxel-wise approach prone to noise-related inaccuracies.

We exploit the regularization of $\mathbf{A}$ and $\mathbf{B}$ to cope with noise and to achieve more accurate estimates thereof. We start from the observation that thanks to a typical tissue structure in the scanned body, the parameters (i.e., elements of matrices $\mathbf{A}, \mathbf{B}$) often do not change rapidly in space. Therefore, square pixel blocks of a proper size behave as low-rank matrices, on average. Likewise, in the time direction, values of neighbouring pixels corresponding to the same tissues behave similarly, i.e. they are likely to form a low-rank structure. This justifies the regularization terms in (1), described next.

The operators D_A^i indexed by i are the "blocking operators", serving to split $\mathbf{A}$ into non-overlapping cube blocks of identical size and forming a matrix by stacking the columns of the cube (so-called Casorati matrix). The operators D_B^j are used to split $\mathbf{B}$ in a similar fashion, but the size of the blocks can be different than in the case of $\mathbf{A}$. The norm $\|\cdot\|_*$

is the nuclear norm, which is the closest convex surrogate to the rank of the matrix [16]. Different scales of $\mathbf{A}$ and $\mathbf{B}$ are taken into account by the user-defined positive weights λ_A and λ_B. The described blocking operators not only provide the desired local low rank behaviour, but they also permit significantly faster computing times than when the entire $\mathbf{A}$ and $\mathbf{B}$ were assumed low rank.

The problem (1) can be shown not to be convex and thus any numeric algorithm for solving the problem might provide a local optimum only. We solve (1) using the proximal gradient method, which can be understood as a generalization of descent methods in the presence of non-smooth regularizers [17]. The algorithm first moves the current estimates of $\mathbf{A}, \mathbf{B}$ in the direction of the negative gradient of the first term; here, a line search is applied, in each variable separately. After the gradient steps, the algorithm adjusts the current estimates such that they form low-rank matrices; this is done using the singular value thresholding [9, 18, 19]. These two principal steps repeat iteratively. The algorithm can be stopped after a finite number of iterations or it can terminate after a heuristic convergence criterion is met. Note that in order to avoid blocking artifacts in the reconstruction, the blocking operators pseudo-randomly shift the blocks in the course of iterations.

3. EXPERIMENTS AND RESULTS

3.1. Pharmacokinetic phantom

Direct evaluation on real DCE-MRI data is not possible because of unknown ground truth. Instead, we evaluated the method on realistic data simulated using our own simulation software PerfSim. The software can generate simulated preclinical DCE-DSC-MRI data and the corresponding pre-contrast data (for the conversion of the DCE image sequence to the CA concentration sequence, see below). The tissue structure of the phantom (1024×1024 pixels) consists of homogeneous tissue regions segmented from a real DCE-MRI dataset (axial slice, head) of a tumor-bearing rat (Fig. 1 left) with the corresponding perfusion parameters assigned based on the real DCE-MRI measurement and the literature. The DCE and DSC components were generated using the Adiabatic Tissue Homogeneity (ATH) pharmacokinetic model [20] and the gradient-correction model according to [4].

The MGE acquisition was simulated with the following parameters: FA = 30°, TR = 15 ms, TE = $\{1, 3, 5, 7, 9, 11\}$ ms. Cartesian k-space data with matrix size 128×96 and 400 time frames with a sampling period of 1.44 seconds were reconstructed using the inverse FFT. The multi-FA pre-contrast data was simulated with FA = $\{3, 5, 10, 15, 20, 25, 30\}$ ° and 20 frames. Coil-element sensitivity maps of a surface 4-channel rat head coil derived from a real DCE-MRI dataset were used.

Five datasets with the above mentioned parameters were generated, varying in the level of the Gaussian noise added to the raw echo signals. The selected standard deviations
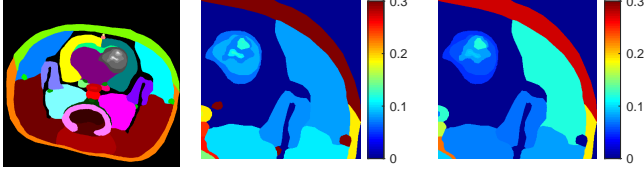
Fig. 1. Structure of the phantom (left, colors identify different tissues) with the tumor depicted in shades of gray and the temporal muscle shown in cyan in the upper right part of the phantom; ground truth maps of F_p [mL/min/mL] (middle); ground truth maps of v_e [mL/mL] (right).

(SDs) for the noise were 0.0001, 0.00025, 0.0005, 0.00075 and 0.001 (for comparison, we measured the noise level from real recordings with a 9.4T MR scanner on a rat in the same region as in our phantom with acquisition parameters mentioned above, but with a dedicated 8-channel surface coil, and obtained SD=0.0001; hence we simulated worse scenarios with e.g. lower field strengths and less specialized coils).

3.2. Computations

Phantom data was fed as $|\mathbf{X}_k|$ into model (1), from where estimates of $\mathbf{A}$ and $\mathbf{B}$ were obtained. For the estimation, 20 iterations of the proximal gradient algorithm with a line-search were run. Different hyperparameter settings were tested: We varied the values of λ_A and λ_B, as well as the sizes of the blocks extracted by operators D_A^i and D_B^j. We preselected a subset of such a grid of hyperparameters, based on the goodness of the fit of $\mathbf{A}$ and $\mathbf{B}$ to their ground truth counterparts. We computed all perfusion maps corresponding to this restricted set and selected the 'optimal' hyperparameters as those which provide the lowest error in the domain of perfusion parameters. The results presented below correspond to such a combination. Naturally, the five different noise levels required five optimal hyperparameter selections.

The estimates obtained using the baseline method and the proposed method were used as the input to the further steps of simultaneous DCE-DSC-MRI perfusion analysis, implemented according to [6, 7]: First, the DCE component, $\mathbf{A}$, was combined with the simulated pre-contrast images to convert the T1-weighted image sequence to the image sequence of CA concentration. Subsequently, the ATH model was fitted to this sequence simultaneously with fitting the gradient-correction model [4] (sharing some parameters with the ATH model) to the DSC component $\mathbf{B}$. This simultaneous fitting was done for each voxel separately. Finally, the maps of perfusion parameters were used for evaluation. The selected perfusion parameters were: blood plasma flow F_p, blood plasma volume v_p, permeability-surface-area product PS, extravascular-extracellular-space (EES) volume v_e, and T2* relaxivities of the plasma and EES compartments r_{2p}^*, r_{2e}^*.

The estimation error is computed as follows: 1/ Each of the two ROIs we chose (muscle and tumor, see Fig. 1) was
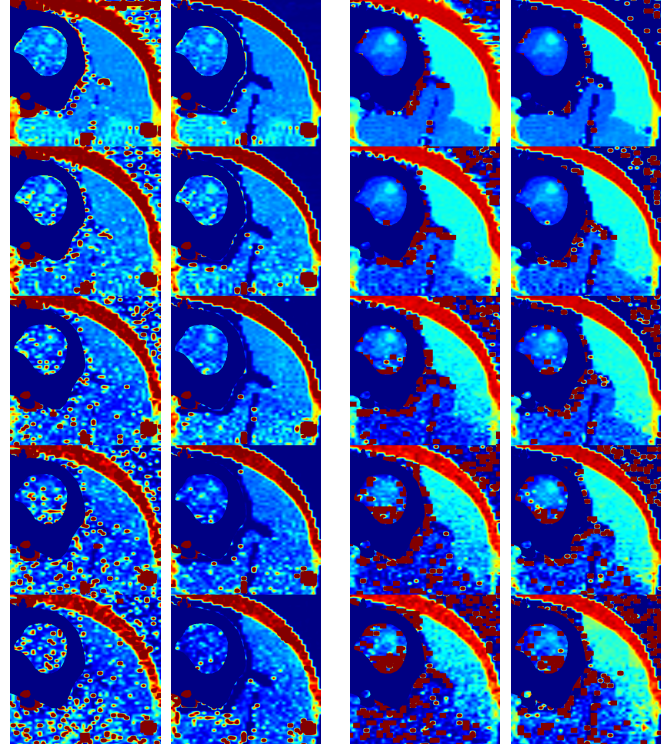

Fig. 2. Resulting perfusion maps. Column 1: F_p – voxel-based method, column 2: F_p – regularized method, column 3: v_e – voxel-based method, column 4: v_e – regularized method. Individual rows correspond to the noise level, increasing from top (SD=0.0001) to bottom (SD=0.001). Color coding corresponding to the scale of images in Fig. 1. Normal-brain region is masked out.

subject to morphological erosion. This had to be done due to the incompatibility of spatial resolutions; our experiments were carried out on 128×96 images, while the original phantom is 1024×1024. The erosion secured that the pixels analyzed further were truly inside the ROI. 2/ For each pixel in a ROI, relative errors (in %) were computed w.r.t. the six ground-truth perfusion parameters. 3/ Median relative errors across the entire ROI were taken for the six parameters.

3.3. Results

The regularized method improves the quality of perfusion maps compared to the voxel-based method, leading to a more homogeneous muscle region and more distinct structures of the brain tumor with fewer outliers (Fig. 2). Quantitative evaluation in the muscle and tumor regions (Tables 1, 2, Figs. 3, 4) shows the same trend, with the improvement being more pronounced in the higher noise regimes. The estimation errors are higher for the tumor, most probably because of its heterogeneity, simulated as several small regions (Fig. 1), which yields partial-volume artifacts (voxels covering multiple regions).

Table 1. Median relative error in the muscle ROI w.r.t. ground-truth parameters; the suffixes 'v' and 'r' of the perfusion-parameter symbols mean 'voxel-based' and 'regularized', respectively

Noise SD	λ_A	λ_B	bl.size **A**	bl. size **B**	F_p**v**	F_p**r**	PS**v**	PS**r**	v_e**v**	v_e**r**	v_p**v**	v_p**r**	r_{2p}^***v**	r_{2p}^***r**	r_{2e}^***v**	r_{2e}^***r**
0.00010	0.0001	0.01	15	5	**5.3**	5.5	**4.2**	4.3	1.4	1.4	**5.2**	5.3	5.4	**5.2**	**2.7**	2.8
0.00025	0.0001	0.1	25	10	9.8	**9.3**	**4.3**	4.9	2.8	**2.7**	7.7	**6.8**	6.4	**5.8**	6.6	**6.5**
0.00050	0.0001	0.1	10	5	20.1	**8.5**	**6.9**	7.1	6.9	**4.3**	13.2	**8.7**	8.2	**6.2**	13.2	**6.7**
0.00075	0.0001	0.1	5	10	28.7	**17.8**	11.6	**9.2**	12.2	**5.8**	25.0	**12.4**	10.1	**7.3**	16.4	**11.0**
0.00100	0.0010	0.1	15	15	34.0	**19.3**	20.2	**12.9**	17.6	**11.8**	33.1	**32.2**	14.3	**10.4**	22.2	**18.0**

Table 2. Median relative error in the tumor ROI w.r.t. ground-truth parameters; the suffixes 'v' and 'r' of the perfusion-parameter symbols mean 'voxel-based' and 'regularized', respectively

| Noise SD	λ_A	λ_B	bl.size **A**	bl. size **B**	F_p**v**	F_p**r**	PS**v**	PS**r**	v_e**v**	v_e**r**	v_p**v**	v_p**r**	r_{2p}^***v**	r_{2p}^***r**	r_{2e}^***v**	r_{2e}^***r**
0.00010	0.0001	0.01	15	5	13.8	**12.8**	30.8	**30.2**	6.5	**6.2**	16.9	**16.5**	12.6	**12.0**	5.8	5.8
0.00025	0.0001	0.1	25	10	25.0	**22.4**	**31.5**	33.8	**9.8**	9.9	22.2	**17.8**	13.5	**10.6**	10.2	**9.1**
0.00050	0.0001	0.1	10	5	39.2	**24.5**	**27.5**	31.7	18.0	**14.5**	26.1	**19.2**	15.5	**8.1**	18.8	**9.4**
0.00075	0.0001	0.1	5	10	42.6	**38.1**	**24.0**	31.7	39.5	**23.7**	34.3	**25.2**	29.9	**9.6**	38.9	**19.4**
0.00100	0.0010	0.1	15	15	52.6	**48.8**	**30.4**	32.6	58.6	**34.8**	39.7	**36.7**	38.9	**13.5**	58.9	**33.9**
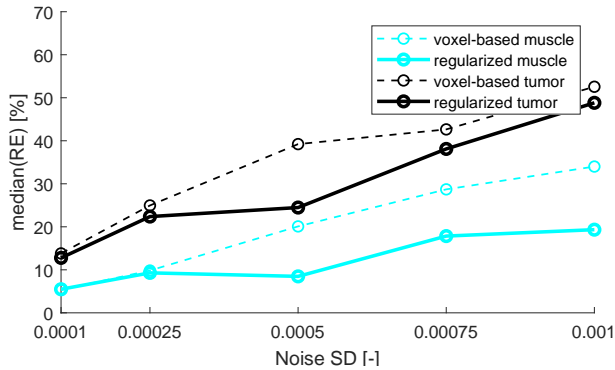
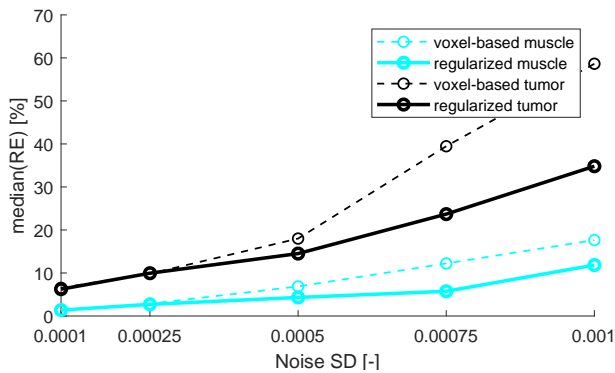**Fig. 3**. Median of relative errors (RE) for F_p in muscle and tumor regions.

Fig. 4. Median of relative errors (RE) for v_e in muscle and tumor regions.

4. DISCUSSION AND CONCLUSION

This contribution presents an improvement of the first step in simultaneous DCE-DSC-MRI processing, i.e., the extraction of the DCE and DSC components from the MGE data. The effect of this step on the whole DCE-DSC-MRI processing chain was evaluated on a realistic synthetic perfusion phantom, including the simulation of the acquisition process. The results show a clear enhancement of the perfusion-parameter maps obtained with the proposed regularized method compared with the baseline method.

In this paper, only magnitude images of the reconstructed MGE data were processed because often, on commercial clinical systems, the data are available only in this form. However, Gaussian additive noise is present in the complex images (as correctly simulated here) and its distribution is changed by the (nonlinear) magnitude operation to the Rician distribution. To account for this, the exponential (i.e. two-parameter) model of the intensity-versus-TE curves is often extended by adding a constant factor as the third parameter. Such an extended model is known to be more suitable especially in regions with a high level of noise and low image intensity and it is planned to be included in the proposed method in the follow-up work. An alternative approach is to model the complex image data; however, this is possible at the cost of an even more complicated model involving the phase image component.

In our evaluation, the observed effect of regularization might be affected by differences in the reconstruction of $|\mathbf{X}_k|$ (use of sensitivity maps in the proposed method versus standard sum-of-squares reconstruction in the baseline method). The effect of this factor will need to be studied separately.

The follow-up work will also include an illustration of the method on real DCE-DSC-MRI data and a possible extension to include image reconstruction from undersampled data. This would make it possible to extend the method from 2D (one slice) to 3D scanning.

5. REFERENCES

[1] Alan Jackson, David L. Buckley, and Geoffrey J. M. Parker, *Dynamic Contrast-Enhanced Magnetic Resonance Imaging in Oncology*, Springer Science & Business Media, Berlin, 2006.

[2] N. Obad, H. Espedal, R. Jirik et al. "Lack of functional normalisation of tumour vessels following anti-angiogenic therapy in glioblastoma," *Journal of Cerebral Blood Flow & Metabolism*, vol. 38, no. 10, 2018.

[3] S. Sourbron, M. Heilmann, A. Biffar, C. Walczak et al. "Bolus-tracking MRI with a simultaneous T1- and T2*-measurement," *Magnetic Resonance in Medicine*, vol. 62, no. 3, pp. 672–681, Sept. 2009.

[4] S. Sourbron, M. Heilmann, C. Walczak, J. Vautier et al. "T2*-relaxivity contrast imaging: First results," *Magnetic Resonance in Medicine*, vol. 69, no. 5, pp. 1430–1437, May 2013.

[5] Ondřej Macíček, Radovan Jiřík, and Zenon Starčuk jr., "Joint DCE- and DSC-MRI processing using the Gradient correction model.," in *ISMRM Proceedings 2017*, Honolulu, 2017, p. 136.

[6] Ondrej Macicek, Radovan Jirik, Peter Latta, and Zenon Starcuk Jr., "Combining DCE and DSC-MRI in Arterial Input Function Estimation Using Multi-Channel Blind Deconvolution," *Joint Annual Meeting ISMRM-ESMRMB ISMRT 31st Annual Meeting*, p. 1583, 2022.

[7] R. Jiřík, O. Macíček, J. Vitouš, L. Krátká, E. Dražanová et al. "Simultanous DCE- and DSC-MRI with blind deconvolution - comparison of gradient-correction and pharmacokinetic models," in *ESMRMB Conference*, 2023.

[8] Z. Hu, A. G. Christodoulou, N. Wang, Y. Xie et al. "MR multitasking-based dynamic imaging for cerebrovascular evaluation (MT-DICE): Simultaneous quantification of permeability and leakage-insensitive perfusion by dynamic T1/T*2 mapping," *Magn Reson Med*, vol. 89, pp. 161–176, 2023.

[9] Ricardo Otazo, Emmanuel Candes, and Daniel K. Sodickson, "Low-rank plus sparse matrix decomposition for accelerated dynamic MRI with separation of background and dynamic components," *Magnetic Resonance in Medicine*, vol. 73, no. 3, pp. 1125–1136, 2015.

[10] F. Ong and M. Lustig, "Beyond low rank + sparse: Multiscale low rank matrix decomposition," *IEEE J. Sel. Topics in Sig. Proc.*, vol. 10, no. 4, June 2016.

[11] M. Daňková and P. Rajmic, "Low-rank model for dynamic MRI: joint solving and debiasing," in *ESMRMB*. Berlin: Springer, 2016.

[12] Marie Daňková, Pavel Rajmic, and Radovan Jiřík, "Acceleration of perfusion MRI using locally low-rank plus sparse model," in *Latent Variable Analysis and Signal Separation*, Liberec, 2015, pp. 514–521, Springer.

[13] Ondřej Macíček, Radovan Jiřík, and Zenon Starčuk Jr., "Comparison of Pharmacokinetic Models for Joint DCE/DSC MRI," in *ESMRMB 2016*, Wien, 2016

[14] M. Uecker, P. Lai, M. J. Murphy, P. Virtue et al. "ESPIRiT – an eigenvalue approach to autocalibrating parallel MRI: Where SENSE meets GRAPPA," Magnetic Resonance in Medicine, Vol. 71, No. 3, 2014.

[15] Per Christian Hansen, Víctor Pereyra, and Godela Scherer, *Least Squares Data Fitting with Applications*, Johns Hopkins University Press, 2013.

[16] B. Recht, M. Fazel, and P. Parrilo, "Guaranteed minimum-rank solutions of linear matrix equations via nuclear norm minimization," *SIAM Review*, vol. 52, no. 3, pp. 471–501, 2010.

[17] P.L. Combettes and J.C. Pesquet, "Proximal splitting methods in signal processing," *Fixed-Point Algorithms for Inverse Problems in Science and Engineering*, vol. 49, pp. 185–212, 2011.

[18] Emmanuel J. Candès, Xiaodong Li, Yi Ma, and John Wright, "Robust principal component analysis?," *J. ACM*, vol. 58, no. 3, June 2011.

[19] Marie Daňková and Pavel Rajmic, "Debiasing incorporated into reconstruction of low- rank modelled dynamic mri data," in *Proceedings of the third international Traveling Workshop iTWIST'16*. Aalborg, 2016, pp. 53–55.

[20] Steven P. Sourbron and David L. Buckley, "Classic models for dynamic contrast-enhanced MRI," *NMR in Biomedicine*, vol. 26, no. 8, pp. 1004–1027, 2013.

[21] X. Wang, Z. Tan, N. Scholand, V. Roeloffs, and M. Uecker, "Physics-based reconstruction methods for magnetic resonance imaging," *Philosophical Transactions of the Royal Society A: Mathematical, Physical and Engineering Sciences*, vol. 379, no. 2200, 2021.